THE AMERICAN SOCIETY OF MECHANICAL ENGINEERS
345 E. 47th St., New York, N.Y. 10017

96-GT-543

ASPIRATING PROBE MEASUREMENTS OF THE UNSTEADY TOTAL TEMPERATURE FIELD DOWNSTREAM OF AN EMBEDDED STATOR IN A MULTISTAGE AXIAL FLOW COMPRESSOR

N. Suryavamshi, B. Lakshminarayana and J. Prato
Center for Gas Turbines and Power
The Pennsylvania State University
University Park, PA 16802

ABSTRACT

The results from the area traverse measurements of the unsteady total temperature using a high response aspirating probe downstream of the second stator of a three stage axial flow compressor are presented. The measurements were conducted at the peak efficiency operating point. The unsteady total temperature data is resolved into deterministic and unresolved components. Hub and casing regions have high levels of unsteadiness and consequently high levels of mixing. These regions have significant levels of shaft resolved and unresolved unsteadiness. Comparisons are made between the total temperature and the total pressure data to examine the rotor 2 wake characteristics and the temporal variation of the stator exit flow. Isentropic efficiency calculations at the midpitch location show that there is about a 4% change in the algebraically averaged efficiency across the blades of the second rotor and if all the rotor 2 blades were behaving as a "best" blade, the improvement in efficiency would be about 1.3%. An attempt is made to create a composite flow field picture by correlating the unsteady velocity data with temperature and pressure data.

NOMENCLATURE

C and n	Hot-wire calibration constants
C_{pt}	Total pressure coefficient (defined as $C_{pt} = \frac{(P_o - \overline{P_{s1}})}{(P_{o1} - P_{s1})}$
$DS2$	Downstream of stator 2
E	Hot-wire output voltage
N_b	Number of blades per rotor
N_{pb}	Resolution of a blade passage
N_{rev}	Number of revolutions of data acquired
P_o	Total pressure
P_r	Total pressure ratio
P_s	Static pressure
PS	Pressure side
r	Recovery factor for hot-wire
RMS	Root mean square value
SS	Suction side
T	Rotor blade passing period
T_o	Total temperature of flow
T_{or}	Total temperature rise
T_{orijk}	Instantaneous total temperature rise
$(T_{orjk})_s$	Ensemble averaged total temperature rise
T'_{orijk}	Unresolved component of total temperature rise
$\overline{T_{or}}$	Time averaged total temperature rise
$(T_{orjk})_{BA}$	Blade aperiodic component of total temperature rise
$(T_{ork})_{BP}$	Blade periodic component of total temperature rise
$(T_{orj})_{RA}$	Revolution aperiodic component of total temperature rise
$(T_{orjk})_{RP}$	Revolution periodic component of total temperature rise
T_r	Total temperature ratio
T_{wi}	Hot-wire temperature
U_t	Blade tip speed
V	Denotes velocity
γ	Ratio of specific heats
η_{isen}	Isentropic efficiency
τ	Fraction of rotor blade passing period

Subscripts:

1	Inlet to IGV
i	Indicates number of hot-wire, Also ensemble averaging index indicating rotor revolution
j	Ensemble averaging index indicating rotor blade count
k	Ensemble averaging index indicating position in rotor blade passage
l	Indicates local value
r	Denotes radial component
x	Denotes axial component

Presented at the International Gas Turbine and Aeroengine Congress & Exhibition
Birmingham, UK — June 10-13, 1996
This paper has been accepted for publication in the Transactions of the ASME
Discussion of it will be accepted at ASME Headquarters until September 30, 1996

θ	Denotes tangential component

Superscripts:

$-$	Denotes time average
$=$	Denotes passage average

INTRODUCTION

Knowledge of both steady and unsteady temperature in turbomachinery is essential for accurate assessment, analysis, and design. One of the approaches suggested for multistage turbomachinery design and analysis is based on the average passage equations of Adamczyk (1985). Several other approaches are still evolving. The apparent heat-flux terms which are analogous to turbulent heat-flux terms in the energy equation of the average passage system of Adamczyk (1985) are responsible for redistribution and spanwise mixing in multistage turbomachinery. These terms are presently either neglected or modeled with ad-hoc constants. The purpose of the research at Penn State is to acquire unsteady temperature data in a multistage axial flow compressor and through analysis provide a scientific basis for the modeling of these terms, which can then be incorporated into the Navier-Stokes design or analysis codes.

Time-resolved measurement of fluid total temperature in a turbomachinery environment has always been a very difficult task. Conventional thermocouples have a frequency response less than 1 kHz while compensated thermocouples are yet to be demonstrated. Constant current hot-wire techniques are also limited to low frequencies unless the fluctuations are small compared to the mean. Electronically compensated, thin-wire resistance thermometers operated at very low overheat ratios have been used to measure temperature at 5 to 10 kHz. However, these techniques are not easily extendable to high speed compressible flows with high dynamic pressure such as those found in turbomachinery configurations. Ng and Epstein (1983) reported the development of a piggy-backed high frequency total temperature probe (aspirating probe) for use in unsteady compressible flows. Kotidis and Epstein (1991) and Alday et al. (1993) have used the aspirating probe to measure the time-resolved total temperature and pressure in transonic compressors. Van Zante et al. (1994) improved the original design of the aspirating probe of Ng and Epstein (1983) by using platinum iridium alloy hot wires and spreading the calibration space to measure both the instantaneous total temperature downstream of a transonic axial flow compressor rotor. The main advantage of the this probe over the earlier ones is that data from the two hot-wires alone is used to obtain the total temperature which reduces the size of the probe and consequently the blockage. It is this configuration with tungsten hot-wires that is used in the present investigation. The main objectives of the research reported in this paper is to understand the nature of the unsteady total temperature field downstream of an embedded stator of a multistage axial flow compressor.

TEST FACILITY, INSTRUMENTATION AND DATA ACQUISITION SYSTEM

The test compressor is a three stage axial flow compressor consisting of an inlet guide vane row and three stages of rotor and cantilevered stator blading with a rotating hub drum. Table I gives the general specifications of the research compressor. The

Table 1. General specifications of test compressor

Number of Stages	3
Tip Diameter	0.6096 m
Hub Diameter at inlet	0.5075 m
Hub Diameter at exit	0.5232 m
Blade Count (rotor)	70, 72, 74
Blade Count (stator)	71, 73, 75
Design Corrected Rotor speed	5410 rpm
Design Corrected Mass Flow	8.609 kg/s
Design Overall Total Pressure Ratio	1.354
Mass Averaged Peak Efficiency at 100% Corrected Speed (Torque Based)	90.65%
Blade Tip Mach Number	0.5
Average Reynolds Number (Based on Stator 3 chord length and axial velocity)	2.448×10^5
Average Hub-Tip Ratio	0.843
Diffusion factor (avg)	0.438
Average Stage Flow Coefficient (V_x/U_t)	0.509
Reaction (avg)	0.570
Space Chord Ratio (avg)	0.780
Aspect Ratio (avg)	1.500
Average Rotor Tip Clearance (static)	1.328 mm
Average Rotor Tip Clearance (dynamic)	0.667 mm
Average Stator Hub Clearance (static)	0.686 mm

test facility is equipped with a stepper motor driven area traverse mechanism. This traverse has three degrees of freedom: radial, circumferential and probe rotation. The probes are inserted into the compressor casing through teflon shoes and the chamber is sealed to prevent flow from recirculating through the slots. The motors are controlled by an IBM compatible 486 personal computer. Approximately 185% of the stator 2 blade pitch can be traversed at each radial location (only 100% of the stator 2 pitch was traversed for this case). The traverse can be axially moved such that area traverses can be conducted downstream of stators 2 and 3 and rotor 3. Lakshminarayana et al. (1994) and Suryavamshi et al. (1994) give a complete description of the test compressor, associated instrumentation, operating characteristics, blade profile geometries and area traverse locations. All the measurements reported in this paper were acquired at the *peak efficiency* operating condition.

The high speed data was acquired using the Metrabyte DAS-50 system. The DAS-50 system was triggered using the once-per-rev pulse from an encoder mounted on the compressor shaft. A signal based upon the resolution of the rotor 2 blade passage (20 points per blade passage) obtained from a disc mounted on the same encoder is used to provide the clock frequency (approximately 130 kHz for this traverse) for the data acquisition system. At each location approximately 3.37 seconds (300 rotor revolutions) of data was acquired. Also a continuous stream of data was acquired at a few locations at a frequency of 200 kHz to conduct a spectral analysis of the data. A 19 by 17 mesh (19 tangential nodes and 17 radial nodes) across one blade passage at stator 2 exit (5.6%

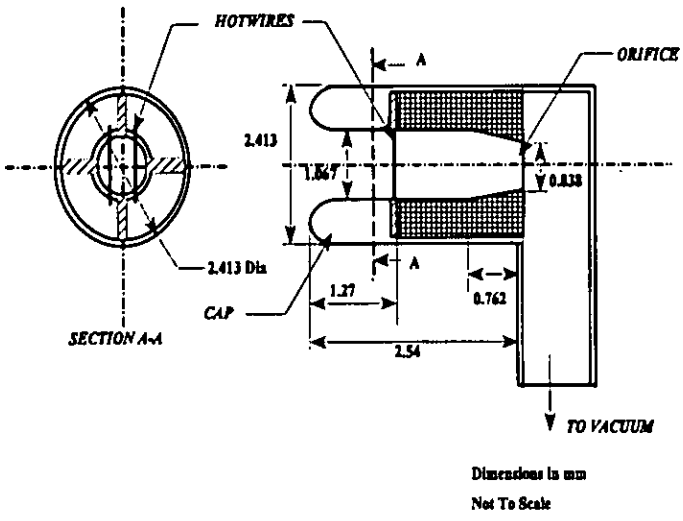

Figure 1. Schematic Drawing of the Aspirating Probe

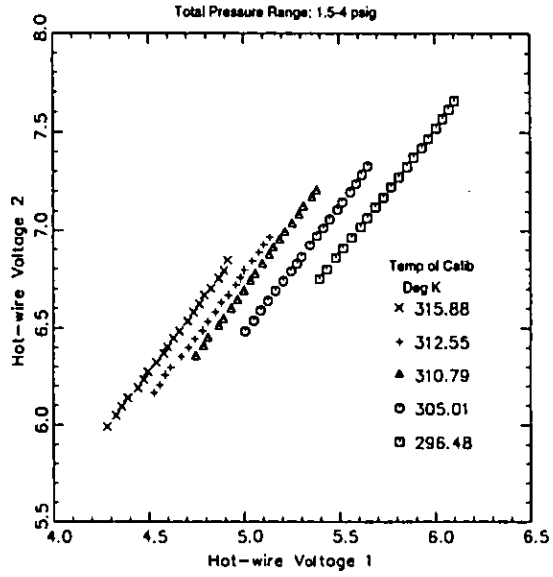

Figure 2. Calibration Space of Aspirating Probe

chord downstream of the stator trailing edge) with clustering in the endwall and the wake regions was employed to resolve the flow field. At each radial location the aspirating probe was rotated to align it in the direction of the mean flow as measured by a pneumatic five hole probe.

Aspirating Probe

The principle of operation involves operating 2 coplanar hot-wires at different overheat ratios (different wire temperatures) in a channel of a choked orifice. Detailed description of the working of the probe is given by Ng and Epstein (1983) and Van Zante et al. (1994). The governing equation of the aspirating probe is given by:

$$E_i^2 = \left[C_i\left(\frac{P_0}{\sqrt{T_0}}\right)^{n_i}\right](T_{wi} - rT_0) \qquad (1)$$

The design of the aspirating probe was obtained from Dr. Ng (1990). This was scaled down to reduce interference effects in the multistage compressor environment. The final channel dia and the choked orifice dia were then scaled such that the Mach number at the wire plane during operation (with the orifice choked) would be approximately 0.40 (the average Mach number of the flow in the compressor). The schematic drawing of the aspirating probe is shown in Fig. 1. The spectrum of the hot-wire voltages show that eight harmonics of rotor blade passing frequency (all three rotors) were captured and the combined frequency response was about 40 kHz (Suryavamshi (1996)).

A static calibration of the aspirating probe is considered adequate since the frequency response of the probe is high. The calibration requires measurement of the dc output voltage from each hot-wire for a range of pressures and temperatures of the pressure and temperature controlled tank. The calibration is performed at a constant temperature of the tank at various tank pressures and at each point, the pressure, temperature and the 2 hot-wire voltages are recorded. The data is reduced and the calibration constants (C_1 , C_2 , n_1 *and* n_2) are calculated. The wire overheat ratios were set at 1.5 and 1.8 (to spread the calibration space) which gave pulse responses of 50.0 and 83.2 kHz respectively. The probe was calibrated through a range of temperatures consistent with the approximate range of the compressor operating point. The calibration constants are a function of temperature and this functionality (a linear regression model) was used in the iteration loop to solve for the unknowns. The calibration space is shown in Fig. 2. The calibration shows good pressure and temperature sensitivity and the temperature resolution is approximately 0.04 Deg K which is much lower than the uncertainty of temperature measurement which is around 0.5 Deg K.

Equating total pressure from the 2 wires of equation 1 we get:

$$\left[\frac{E_1^2}{C_1(T_{w1} - rT_o)}\right]^{\frac{1}{n_1}} = \left[\frac{E_2^2}{C_2(T_{w2} - rT_o)}\right]^{\frac{1}{n_2}} \qquad (2)$$

A Newton-Raphson iteration technique was used to solve the equation 2. The levels of total pressure unsteadiness derived from the measurement in the multistage compressor were almost twice as that derived from a traverse of the semi-conductor kulite probe at the same location. Until this discrepancy is resolved, it was decided that the aspirating probe would be used to measure total temperature and the kulite probe to measure total pressure.

DECOMPOSITION OF INSTANTANEOUS SIGNAL

Each discrete measurement of total temperature is presented as an instantaneous total temperature rise T_{orijk}.

$$T_{orijk} = (T_{oijk} - \overline{T_{oi}}) \tag{3}$$

Here subscripts i,j, and k represent indices in ensemble averaging (i indicates the index of revolution, j the index of the blade in the row, and k the index of the point in the blade passage). Following the description of Suder et al. (1987) and Suryavamshi et al (1994), the instantaneous total temperature is then decomposed into a shaft resolved (ensemble average,$(T_{orjk})_s$) and an unresolved component (T'_{orijk}).

$$T_{orijk} = (T_{orjk})_s + T'_{orijk} \tag{4}$$

where the ensemble average is given by:

$$(T_{orjk})_s = \frac{1}{N_{rev}} \sum_{i=1}^{N_{rev}} (T_{or})_{ijk} \tag{5}$$

and

$$T'_{orijk} = T_{orijk} - (T_{orjk})_s \tag{6}$$

This shaft resolved component has contributions from viscous and inviscid rotor-stator interaction effects which repeats every revolution. The shaft resolved component is further decomposed into a time average ($\overline{T_{or}}$), a revolution periodic ($(T_{orjk})_{RP}$) and a revolution aperiodic ($(T_{orj})_{RA}$) component as shown in Fig. 3.

$$(T_{orjk})_s = \overline{T_{or}} + (T_{orj})_{RA} + (T_{orjk})_{RP} \tag{7}$$

$$\overline{T_{or}} = \frac{1}{N_{rev} \times N_b \times N_{pb}} \sum_{i=1}^{N_{rev}} \sum_{j=1}^{N_b} \sum_{k=1}^{N_{pb}} T_{orijk} \tag{8}$$

$$(T_{orj})_{RA} = \frac{1}{N_{pb}} \sum_{k=1}^{N_{pb}} [(T_{orjk})_s - \overline{T_{or}}] \tag{9}$$

$$(T_{orjk})_{RP} = [(T_{orjk})_s - \overline{T_{or}} - (T_{orj})_{RA}] \tag{10}$$

The time averaged component describes the steady state flow field which is the same in each blade passage of the blade row. The revolution periodic component describes the temporal fluctuations due to the relative motion between the blade rows and the revolution aperiodic component (which is a passage to passage average) arises from different blade count in successive stages (rotor or stator). For a single stage machine or a multistage machine with the same blade count in successive stages, the revolution aperiodic component identically goes to zero. The revolution aperiodic component generally represents the asymmetry about the circumference in the rotor frame of reference with a time constant of one rotor 2 blade passing period. During analysis of the total pressure data acquired it was found that there are variations in the periodic fluctuations between blades in the same row due to various causes (geometrical, incidence variations, loading changes etc.). Since most of the design principles are based on solving the flow equations for one blade passage, it is essential to determine the periodic unsteadiness for the average rotor passage. This average passage is termed the "blade periodic unsteadiness" and the difference between the revolution periodic and the blade periodic is the "blade aperiodic unsteadiness".

$$(T_{orjk})_{RP} = (T_{ork})_{BP} + (T_{orjk})_{BA} \tag{11}$$

$$(T_{ork})_{BP} = \frac{1}{N_b} \sum_{j=1}^{N_b} [(T_{orjk})_{RP}] \tag{12}$$

$$(T_{orjk})_{BA} = [(T_{orjk})_{RP} - (T_{ork})_{BP}] \tag{13}$$

The blade periodic component ($(T_{ork})_{BP}$) generally represents the fluctuations of the total pressure field over an "average" rotor 2 blade passing period. The blade aperiodic component ($(T_{orjk})_{BA}$) generally represents the asymmetry about the circumference in the rotor frame of reference with a time constant of the sampling period. Since the decomposition of the original signal has already filtered the asymmetries with a time constant on the order of a rotor 2 blade passing period (revolution aperiodic), this component includes short term asymmetries synchronized to the passage of the individual rotor 2 blades. Full details of the decomposition (including the equations used to derive the various components) is given in Suryavamshi et al. (1994) and shown in Fig. 3 for the total pressure signal. While this decomposition is mathematically rigorous (i.e. the unsteady signal can be reconstructed by summing each of the components), it is premised upon the idealized assumption that all of the deterministic structure is synchronized to the shaft rotation. Measurement of the unsteady total temperature field resulting from some deterministic physical phenomena, such as vortices originating in the stationary frame of reference, will be included in the unresolved component. Additionally, variations in the magnitude of the velocity deficit, width, and spatial positions of the rotor wakes between rotor revolutions, which are clearly shaft-synchronized physical phenomena, contribute to the unresolved component. As a consequence, the magnitude of the shaft-resolved and unresolved components of the unsteady temperature signals cannot be explicitly defined as the respective contributions to the total unsteadiness of the deterministic structures and random turbulence. However, this data can be used to identify in which regions of the flow field each of these components make significant contributions to the total unsteadiness and consequently mixing in the compressor.

TIME AVERAGED DATA

Figure 4 shows the blade-to-blade variation of time averaged total temperature rise near the hub, midspan and casing locations. Also shown in this figure are the hub to casing distributions of mass weighted passage averaged values of time averaged total temperature and pressure. The total pressure was acquired using a high frequency total pressure probe. The details of this measurement are given in Suryavamshi et al. (1994). Higher temperatures seen on the pressure side of the stator wake are consistent with the analysis of Kerrebrock and Mikolajczak (1970). This is due to the rotor wake accumulation on the pressure side of a downstream stator. The average variation of temperature between the stator core flow to the stator wake is about 1.0 K which is about 10% of the rotor temperature rise except around 22% span where the

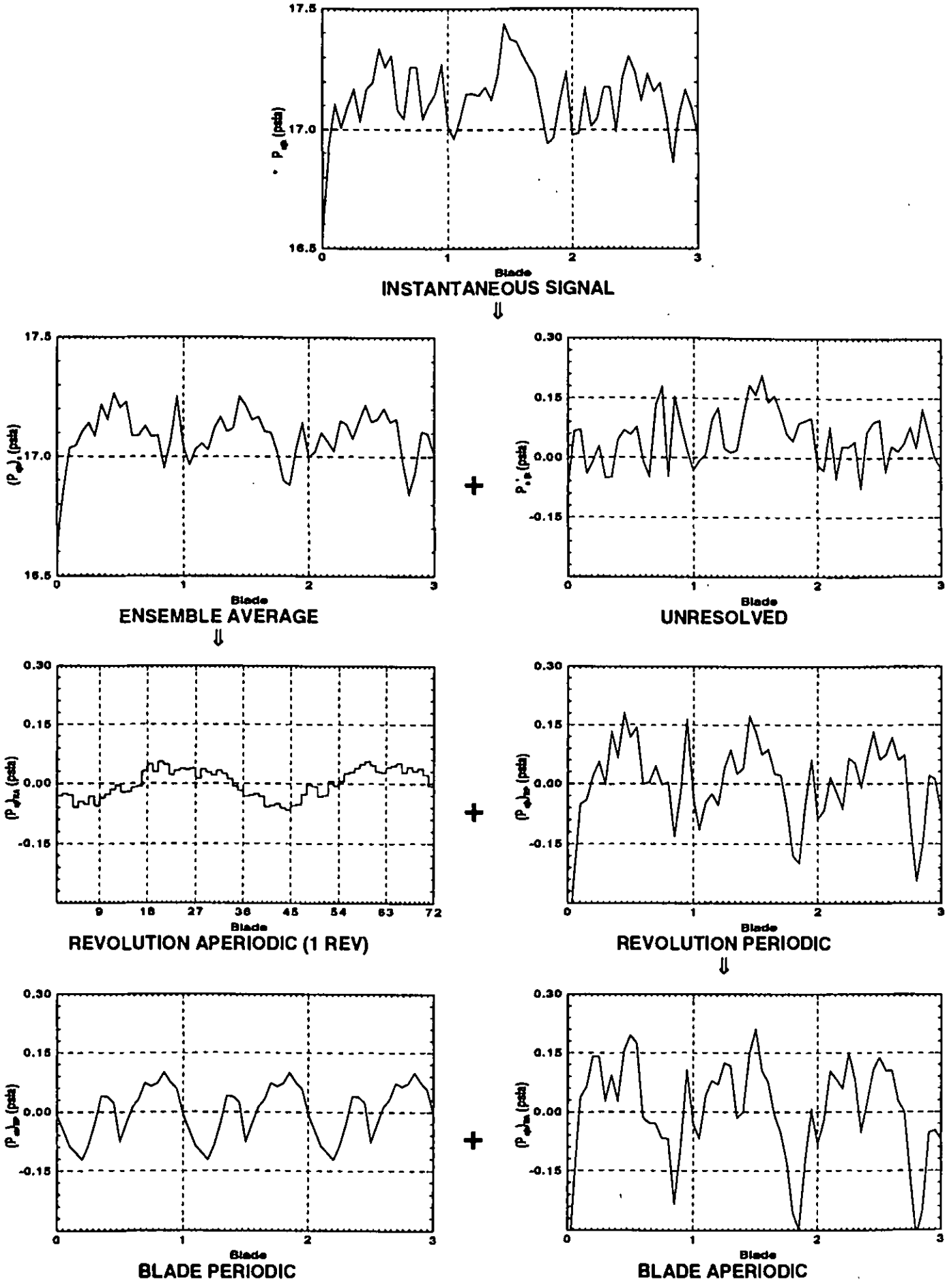

Figure 3. Schematic of decomposition of instantaneous data: Actual total pressure data

variation is around 5.0 K. The endwall flow region with lower pressures and higher temperature, near the casing extends to 70% span while the region near the hub extends to about 15% of the span. The presence of endwall flow as well as interaction with the rotor leakage flow contributes to much lower efficiency in the casing endwall region. Consequently higher temperatures and lower pressures are recorded compared with the hub region.

Figure 5 shows the contours of the time averaged quantities (total pressure coefficient, total temperature rise and isentropic efficiency). The isentropic efficiency is calculated using the following equation:

$$\eta_{isen} = \frac{P_r^{\frac{\gamma-1}{\gamma}} - 1}{T_r - 1} \tag{14}$$

where

$$P_r = \frac{P_{ol}}{\overline{P}_{ol}}, \; T_r = \frac{T_{ol}}{\overline{T}_{ol}} \tag{15}$$

Let us focus on the important features of the flow: the presence of the stator wakes, effect of the secondary flow and the thickening of the boundary layer near the suction surface corner in the casing region. The measurement grid in the endwall regions is denser for the total pressure measurement due to a smaller size of the kulite probe. As a result the radial contouring is smoother for the pressure compared with the temperature data. The interaction of the stator wake flow with the endwall flow features and rotor tip clearance flow causes intense mixing which results in much thicker wakes and very low efficiency in the endwall regions compared with the midspan region. Similar distributions have been measured by Howard et al. (1993). The suction surface-casing endwall corner region of low total pressure due to probable corner stall, inlet skew and casing corner flow does not show much variation in the time averaged total temperature across the passage. This is however, a region of low efficiency and high unresolved unsteadiness (as will be seen later). In the casing endwall region, intense mixing caused by interaction of the rotor tip leakage flow and the casing endwall boundary layer gives rise to almost uniform distribution of pressures, temperatures and consequently efficiency across the blade pitch from 85 to 95% span (last measurement location). Blade-to-blade non-uniformities is observed only near the stator wake regions.

On the pressure side of the stator wake, around 25% span, there is a region of low efficiency, low pressure rise and high temperature rise. This region is probably caused by the accumulation of hubwall boundary layer fluid due to the scraping effect of the blade caused by hub rotation as well as migration of upstream rotor flow towards the pressure surface. This region at its largest almost spans 1/3 of the blade spacing. This could also be caused by the accumulation of fluid due to radial outward transport of the low momentum rotor 2 hubwall corner flow towards midspan by the radial outward velocity at the exit of the rotor. Near the suction side of the stator wake close to the hub, low temperatures, moderate pressure rise and high efficiency is observed. This is probably caused by leakage flow from the hub region augmented by hub rotation washing away the corner separation region. This is also the region of intense flow mixing. This may account for high efficiency observed almost across the entire passage.

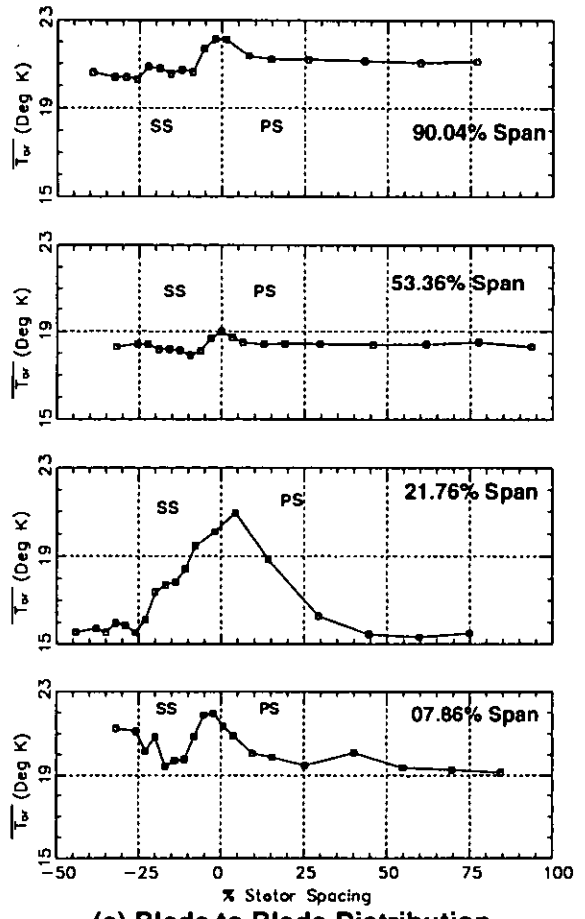

(a) Blade to Blade Distribution

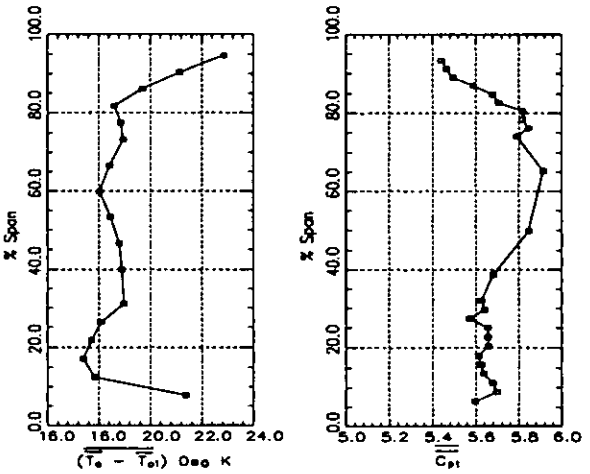

(b) Hub to Tip Variation

Figure 4. Blade-to-blade and hub-to-tip variation of time averaged quantities.

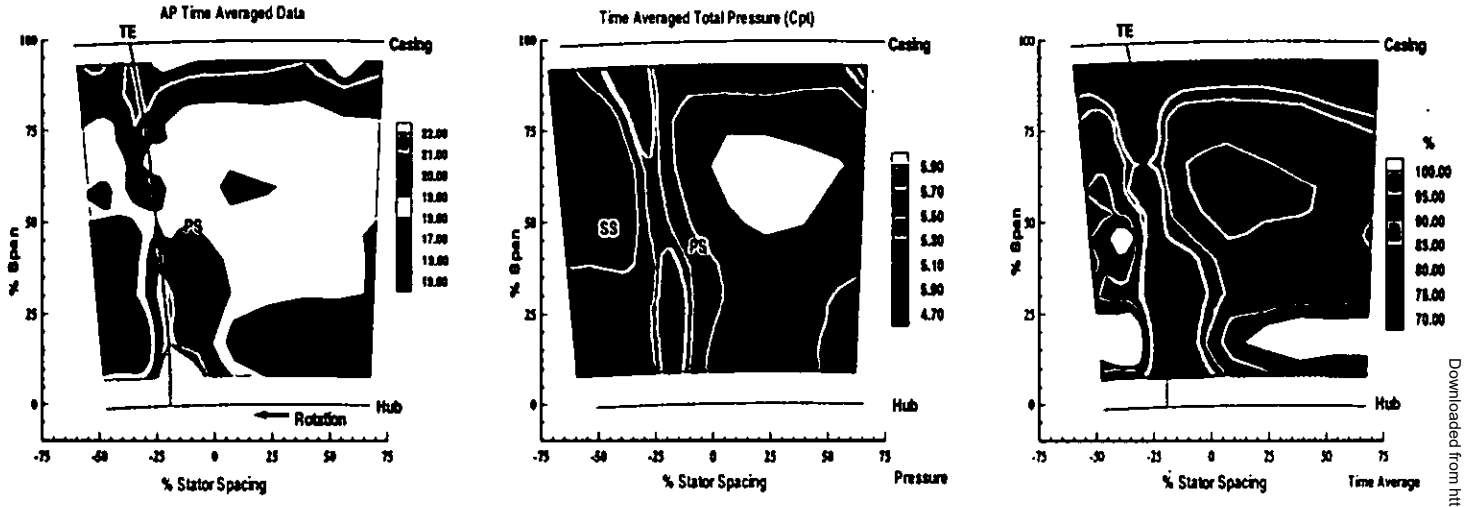

(a) Total Temperature $\overline{T_{or}}$ (b) Total Pressure $\overline{C_{pt}}$ (c) Isentropic Efficiency $\overline{\eta_{isen}}$

Figure 5. Contours of time averaged total quantities: Temperature, pressure and isentropic efficiency.

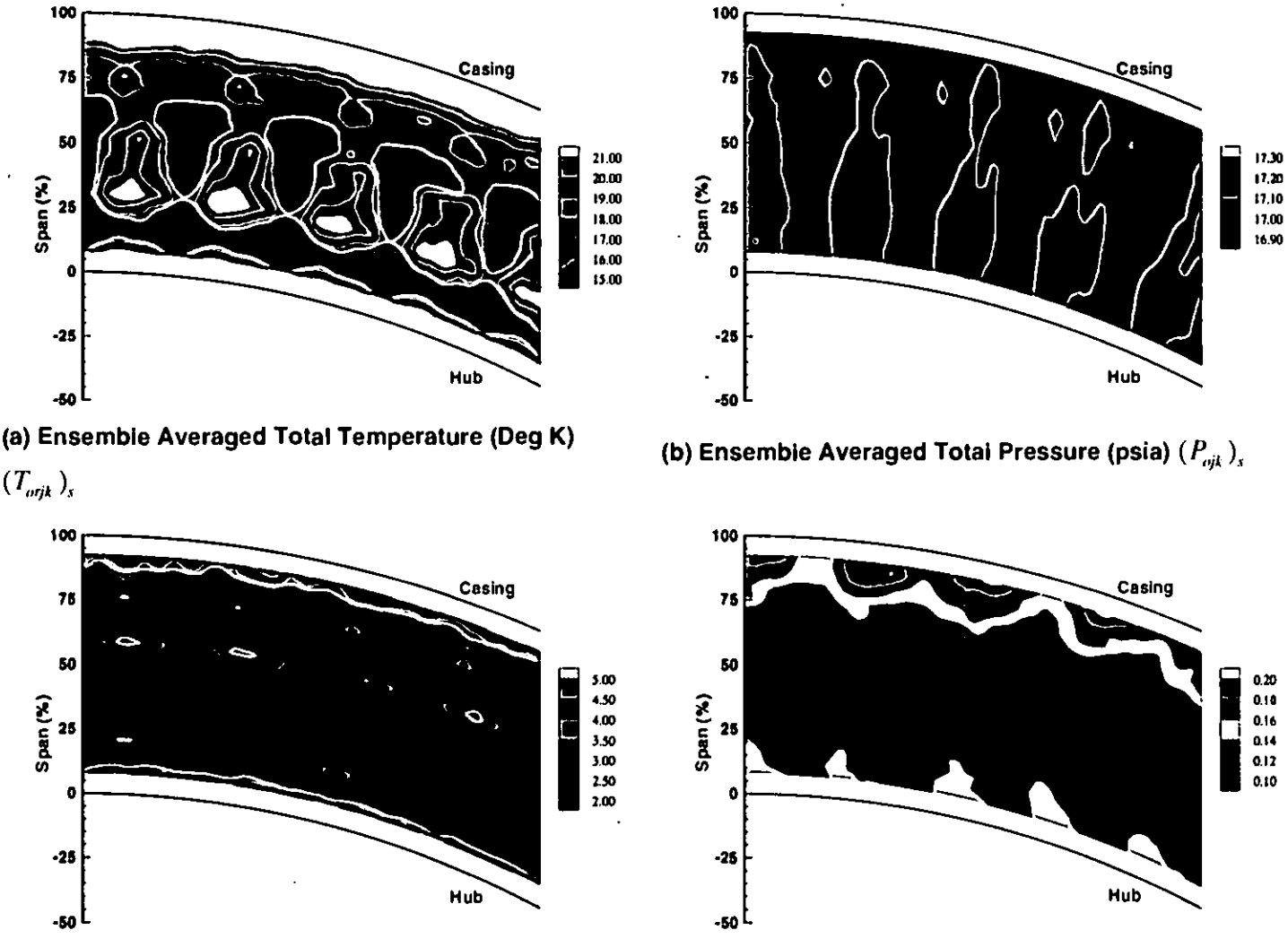

(a) Ensemble Averaged Total Temperature (Deg K) $(T_{orjk})_s$

(b) Ensemble Averaged Total Pressure (psia) $(P_{ojk})_s$

(c) RMS Unresolved Unsteadiness in Total Temperature (Deg K)

(d) RMS Unresolved Unsteadiness in Total Pressure (psia)

Figure 9. Contours of ensemble averaged and RMS unresolved unsteadiness: Rotor 2 exit flow at midpitch.

UNSTEADY DATA

In this section the unsteady total temperature field is presented and analyzed. Unsteadiness at the exit of the stator exists due to interaction of atleast three different mechanisms: the presence of rotor 2 wakes being convected through the stator passage which have not fully mixed out, the shedding of vorticity from the stator trailing edge due to a time varying stator circulation or loading caused by the passage of the rotor wakes over the stator surface, and the presence of the rotor 3 potential field. By analyzing the stator exit data, it is possible to determine which of these mechanisms are dominant contributors to the unsteadiness. Care must be taken when interpreting the unsteady data because of the frequency response limitations of the aspirating probe. The most apparent limitation of these measurements is the resolution of the random turbulent fluctuations which are included in the unresolved component of total temperature. Assuming a mean velocity of 100 m/s, the smallest length scale measured by the probe is given by $100/40000 = 2.5\times10^{-3}$m. Hence energy in turbulent eddies with length scales smaller than this is not measured by the instrument. Therefore the instrument measures all the features associated with frequencies less than 40 kHz (blade passing, shaft frequency and substantial part of random turbulence). For deterministic structure associated with the rotor blades (blade passing frequency of 6.5 kHz for the second rotor), this instrumentation can measure the first six harmonics. Although finer details of the structure may be contained in higher harmonics, beyond the measurement capability of the probe, the majority of the energy content is included in these lower harmonics. 250 revolutions of rotor locked data was used for ensemble averaging. The appropriate number of ensembles to process was determined by examining the differences between averaged signals at the suction surface casing endwall corner region comprised of 10, 20, 50, 100, 150, 200, 250 and 300 revolutions. Assuming exponential decay of difference as a function of number of ensembles, it was estimated that the bias introduced by averaging 125 ensembles was a small fraction of the measurement uncertainty.

The ensemble averaged flow is viewed from three different perspectives in this paper. Firstly attention is focused on the RMS flow field. This gives an overall picture of the unsteady flow field as frozen in time downstream of the stator. Both pressure and temperature plots are used to explain this flow. Then attention is focused on the temporal variation of the stator exit flow at each instant of rotor passage time. This gives the complete picture of how the flow field downstream of the stator is changing with passage of the rotor. For this perspective 6 frames of ensemble averaged and RMS unresolved unsteadiness in total temperature is used. Each frame represents one rotor 2 location with respect to the stator and 20 frames represent one blade passage (only six are shown for the sake of brevity). A movie version of this description is available on the world wide web. The access URL is *http://turbo5.aero.psu.edu/vamshi/movie.html*. This represents the description from the perspective of one rotor blade only. Ensemble averaged total temperature and RMS unresolved unsteadiness in total temperature are used to describe the flow. Comparisons are made to the total pressure field similarly described in Suryavamshi et al. (1994). The results from this description are useful in determining the influence of the stator on the inlet flow to the downstream rotor. Finally, blade-to-blade distributions of the unsteady pressures and temperatures at the midspan, midpitch location are correlated with the unsteady velocity field obtained at the same location using a slanted hot-film probe to derive the composite flow field.

RMS Flow Field

In this section the hub to tip contours of RMS values of the unsteady components of total temperature are presented and analyzed. For each of the unsteady components, the RMS values are calculated by averaging the square of the unsteadiness over their respective time periods (one revolution for revolution periodic and blade aperiodic components, one blade passage for blade periodic, all the blades of rotor 2 for revolution aperiodic and all 250 revolutions for the unresolved component) and normalizing it by the local time averaged total temperature rise. (Similar unsteadiness numbers are expressed for the total pressure data as well). RMS total unsteadiness is calculated by squaring and adding the RMS values of the individual components and taking the square root.

Figure 6 shows the blade to blade variation of RMS unsteadiness in total temperature across the stator pitch at three typical radial locations. This figure shows that the unresolved unsteadiness is much higher than the deterministic unsteadiness in the endwall regions (almost 3 times near the hub (not shown)) but is only marginally higher than the deterministic unsteadiness in the midspan-midpitch region. In the stator wake region, the unsteadiness level is much higher than in the core region of the flow. The width of the stator wake can be clearly seen in this data. A large increase in the unresolved unsteadiness in the stator wake is probably due to the increase in unsteadiness in the stator wake and its interaction with the rotor wake. Similar distributions are seen in the total pressure kulite data and in the slanted hot-film data. As one progresses from hub to casing, there is very little change in the width of the core region on the suction surface, but a significant decrease is seen in the casing endwall region, as the unsteadiness increases in the suction surface casing endwall region, even though the total temperature does not significantly change in this region. The deterministic unsteadiness as seen earlier has been broken down into revolution periodic and aperiodic unsteadiness. The revolution aperiodic unsteadiness which is a measure of the rotor-rotor interaction is almost constant across the pitch at all three radial locations and is much smaller than the revolution periodic unsteadiness at every location. This indicates that the influence of potential field of rotor 3 on the stator exit data is probably very small at this axial station downstream of the second rotor. Further measurements are probably necessary to quantify this much more clearly. The revolution periodic unsteadiness, which is a measure of the periodic rotor wake fluctuations, behaves much like the unresolved unsteadiness in that the wakes show higher periodic fluctuations than in the core flow. The pressure side of the stator wake shows higher fluctuations and larger region affected by rotor-stator interaction than on the suction side except in the casing endwall region. This could be due to the accumulation of the rotor wake fluid on the pressure side of the downstream stator as well as unsteady loading of the stator causing shed vorticity. Similar distributions were also observed in the total pressure data as well.

Figure 7(a)-(f) shows the hub to tip contours of total, unresolved and revolution periodic unsteadiness in total temperature com-

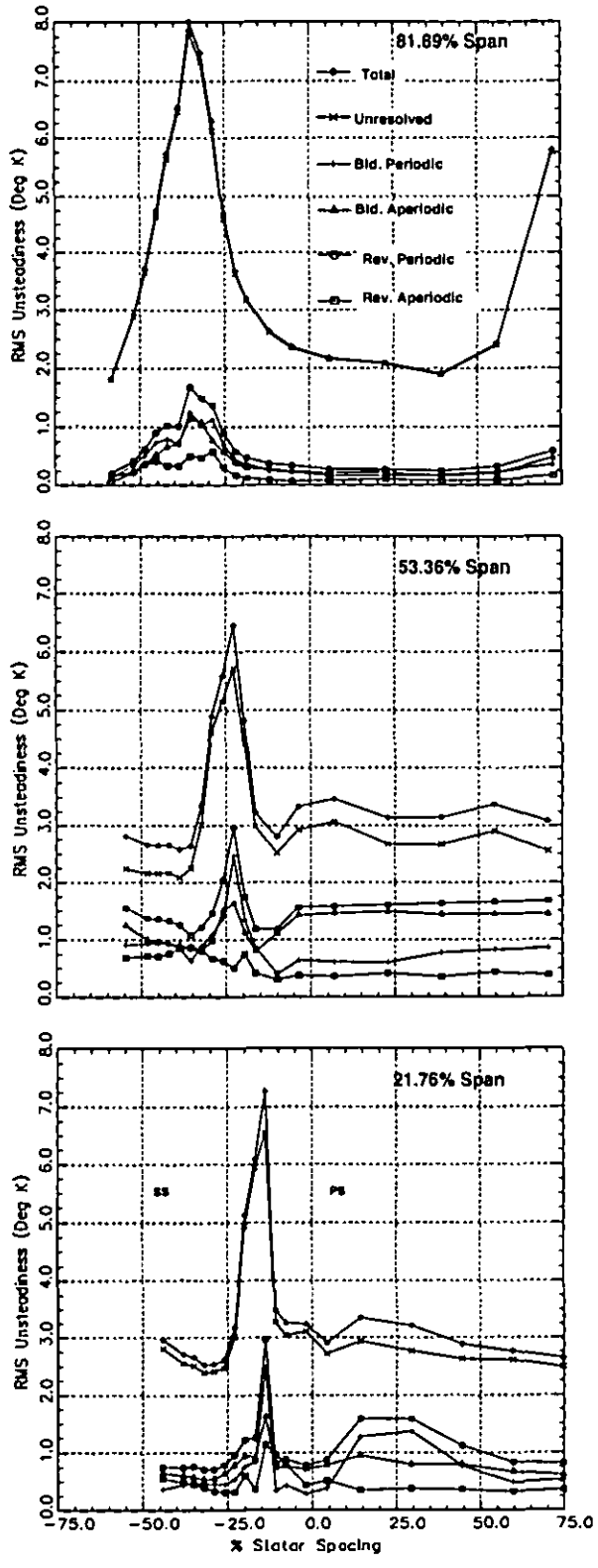

Figure 6. Blade-to-blade variation of time averaged RMS unsteadiness in total temperature rise (deg K)

pared with the respective rms values in total pressure coefficient. Let us start with the total unsteadiness distributions (Fig. 7(a) and (b) and then proceed to the components: unresolved (Fig. 7(c) and (d) and revolution periodic (Fig. 7(e) and (f). Low levels of total unsteadiness in both pressure and temperature is seen in the core region. In addition, the stator wake has higher unsteadiness than the core region, and this is caused by upstream rotor wake, the resulting unsteady stator blade boundary layer and the turbulence in the stator wake. In the casing endwall region on the suction surface, a zone of high unsteadiness is seen in both the plots. This is due to the high levels of mixing present as a result of interaction between the annulus wall boundary layer, secondary flow and the low momentum region on the suction surface endwall corner and the leakage flow from the upstream rotor. The location of this region with respect to the blade passage is almost the same in both the plots, however, the width of this region is different. The total temperature shows a slightly larger region of unsteadiness compared to the pressure data. This could be due to the relatively sparse grid used for the temperature measurement. It is now interesting to progress from the total unsteadiness distribution into the deterministic and the unresolved components. Figures 7(c), (d), (e) and (f) show the deterministic and unresolved unsteadiness distributions for the total temperature and total pressure respectively. The deterministic unsteadiness is represented by the revolution periodic component (which is a combination of both blade periodic and blade aperiodic components). By comparing Figures 7(a) through (f), bulk of the unsteadiness in the endwall regions is unresolved in nature. However, in the core regions of the flow, both deterministic and unresolved unsteadiness are of similar magnitude. The suction surface casing endwall corner zone is mainly unresolved in nature, both the temperature and pressure data seem to confirm this. The deterministic unsteadiness distributions do not show many changes in the wake except on the pressure side of the wake, where slightly higher total temperature and much higher total pressure unsteadiness is seen. This tends to confirm the theory that the rotor wake (which has high levels of periodic unsteadiness) accumulates on the pressure side of the downstream stator. This is not seen very clearly in the temperature possibly because of very low temperature unsteadiness compared with the total pressure at this location. The aspirating probe may not have much sensitivity to resolve such a low temperature difference. The total temperature rise of the second stage is approximately only 10 Deg K, whereas the total pressure rise is approximately 1.6 psia. In addition the wake in the hub region has higher unsteadiness. This is probably caused by transport of both the rotor wake and the stator boundary layer towards the hub, caused by radial pressure gradient.

In the casing endwall region, the temperature distribution shows a drop in the periodic unsteadiness (from the core region) but no such change is seen in the total pressure data. This could be due to a much faster decay of the total temperature unsteadiness in the casing endwall region due to interactions with the annulus wall boundary layers and rotor leakage flow/vortex or it could be due to a smearing of the rotor leakage flow by the stator passage. Also the uncertainty band on the total temperature is much higher than that on the total pressure. In the unresolved unsteadiness distribution, a clear wake is seen in the total temperature data but not in the total pressure data. Possibly due to the larger surface area of averaging

on the kulite total pressure probe, the unsteadiness levels are lower in the total pressure than in the total temperature measurement. The suction surface casing corner endwall region is seen in both the pressure and temperature data. The width of the region is much larger in the temperature data compared to the pressure data. Comparing the deterministic and unresolved unsteadiness distributions, it is clear that the unsteadiness in the suction surface casing endwall corner region is mainly unresolved in nature.

It is interesting to compare Fig. 7 with Fig. 5(c). Regions of high levels of total unsteadiness are regions of very low efficiency (suction surface casing endwall corner region and the stator wake regions). This seems to indicate that higher unsteadiness is associated with mixing of the wakes, leakage flow and secondary flow due to the upstream rotor, essentially a viscous phenomena. Associated with this are losses due to viscous and turbulent dissipation. This results in higher temperature rise, lower pressure rise and lower efficiency. Thin stator wakes and elimination of the casing endwall corner flow regions is the key to increasing the efficiency of the compressor.

Temporal Variation of Stator Exit Flow

The temporal variation of the stator exit flow is discussed in this section. For the sake of brevity, the following discussion is limited to the ensemble averaged and unresolved unsteadiness results only. Figure 8 contains several perspectives of the stator exit measurements "frozen" at the same instant in time within the rotor revolution, but derived by averaging over 250 consecutive rotor revolutions. Six frames from the passage of the first rotor blade across the stator passage is shown but the interpretation is based on the analysis of 20 frames (the first blade in the revolution). A clock in the upper right hand corner of each picture shows the passage of the rotor blade across the stator passage (from $\tau/T = 0.0$ to $\tau/T = 1.0$). Here τ represents the fraction of blade passing period T. These times are arbitrary as the location of the rotor blade with respect to stator is not known. The location of the trigger is the same with respect to all locations in the stator passage. Three regions of the flow are focused on in this discussion: (1). The stator wake region away from the casing endwall, (2). The casing endwall corner region (blade suction surface and casing endwall corner), and (3). Hub endwall flow region.

Stator wake region away from the casing endwall. As the rotor passes across the stator passage there is a change in the behavior of the stator wakes away from the casing endwall. This is best seen in the unresolved unsteadiness distribution. Different behaviors are seen at different radii. Near the hub, the width of the wake decreases from $\tau/T = -0.25$ (not shown) to about $\tau/T = 0.25$ and then starts increasing again. The width is the highest at $\tau/T = 0.75$ and then slowly decreases till $\tau/T = 1.25$ (not shown). The wake is also the deepest (defined by the increase in the rms value of the unresolved unsteadiness) at $\tau/T = 0.75$ and the shallowest at $\tau/T = 0.25$. The depth of the wake decreases from $\tau/T = -0.25$ to $\tau/T = 0.25$ and then increases till $\tau/T = 0.75$. At mid-span however, the width of the wake is almost constant as the rotor passes by. The stator wake depth at midspan shows almost the opposite behavior. The wake is deepest at $\tau/T = 0.25$ and the shallowest at $\tau/T = 0.75$. However, the change in the maximum values of the unresolved unsteadiness in the wake between the two time periods is small. So one can almost say that the wake depth at mid-span does not change very much. This time step ($\tau/T = 0.75$) is termed the "*maximum interaction time*". On the pressure side of the stator the width of the wake (unresolved unsteadiness) is always greater than on the suction side. This is because the rotor wake is being transported towards the pressure side as the rotor passes the stator.

Casing endwall corner region. Like the wake region, this region also changes significantly with rotor passing. This region pulses (increases and decreases in size) as the rotor passes. Similar behavior was observed by Cherrett et al. (1994) in the hub corner flow region downstream of a stator of a single stage transonic fan. The region starts decreasing in size as the time increases from $\tau/T = 0.0$ and is the smallest at $\tau/T = 0.5$ and then starts increasing rapidly reaching a maximum at the maximum interaction time. As time further increases, the region starts decreasing once again in size. This is true for both the ensemble average as well as the unresolved unsteadiness. Cherrett et al. (1994) theorize that this is due to the rotor moving in front of the stator leading edge. The stator wake as we saw earlier was the thickest at $\tau/T = 0.75$. As the region grows in size from $\tau/T = 0.5$ to 0.75, the region is no longer confined to the suction surface region. It slowly spreads to the pressure surface and at $\tau/T = 0.75$, the region is almost the same size on either of side of the stator blade. It is also interesting to see that the corner region is seen to be "feeding" the flow in the casing region away from the endwalls as the blade passes by. This is seen very clearly in the unresolved unsteadiness distribution but not in the ensemble averaged plots.

Hub endwall flow region. This region can be best explained using both the unresolved unsteadiness and the ensemble averaged temperature distributions. Slightly higher levels of unsteadiness seen in between the stator blades very close to the hub is indicative of this region. At $\tau/T = 0.0$ the region is spread out almost across the entire passage and as the rotor moves across the stator blade, the clearance flow grows in size in the spanwise direction while shrinking in the circumferential direction and starts moving across the passage probably transporting some of the hubwall boundary layer flow towards the pressure surface of the stator blade. This can be verified by the appearance of higher levels of unsteadiness on the pressure surface of the blade. It was supposed earlier that there is scraping of the hubwall boundary layer and a presence of scraping vortex (see Prato et al. (1995)). The appearance of high unsteadiness on the pressure surface away from the hub seems to substantiate this notion. And as the rotor blade continues further, the hub clearance region starts decreasing in size in the spanwise direction and starts spreading across the stator passage. The rotor passing has indeed triggered this type of behavior and certainly needs to be modeled for accurate prediction of the stator exit flow fields in a multistage compressor.

From the above discussion it can very clearly remarked that the stator exit flow is controlled by not only the rotor passing but also by the relative location of the rotor with respect to the stator. Very consistent information like the appearance of thick stator wakes and a large casing corner endwall region when the rotor trailing edge is in front of the stator leading edge characterizes the maximum interaction phenomena as well.

Rotor 2 Exit Field at Mid-pitch

In this section, the blade-to-blade distribution of the rotor 2 field

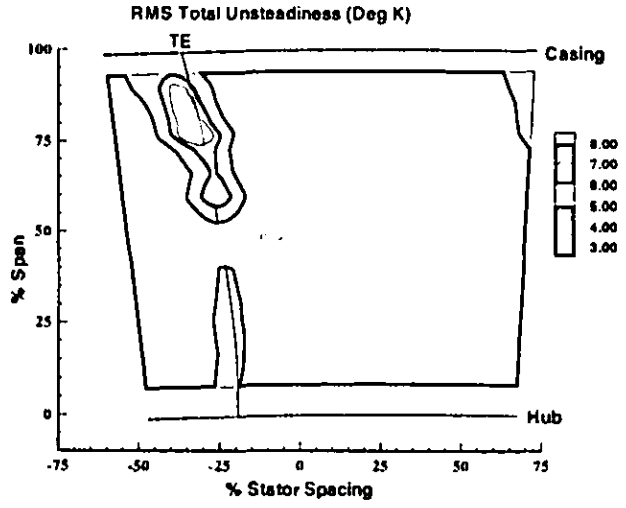

(a) RMS Total Unsteadiness (Deg K)

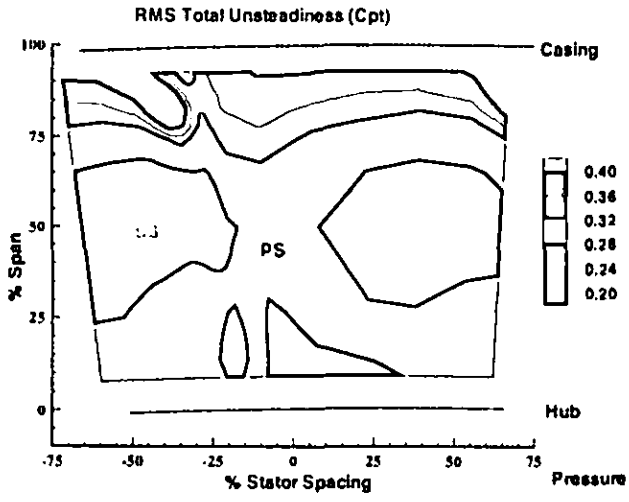

(b) RMS Total Unsteadiness (Cpt)

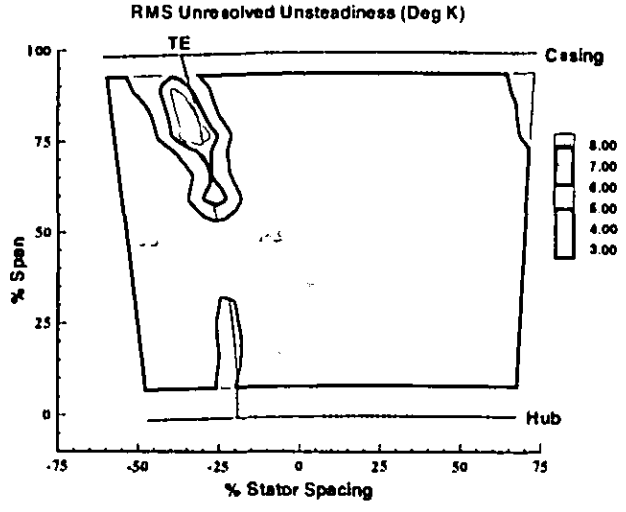

(c) RMS Unresolved Unsteadiness (Deg K)

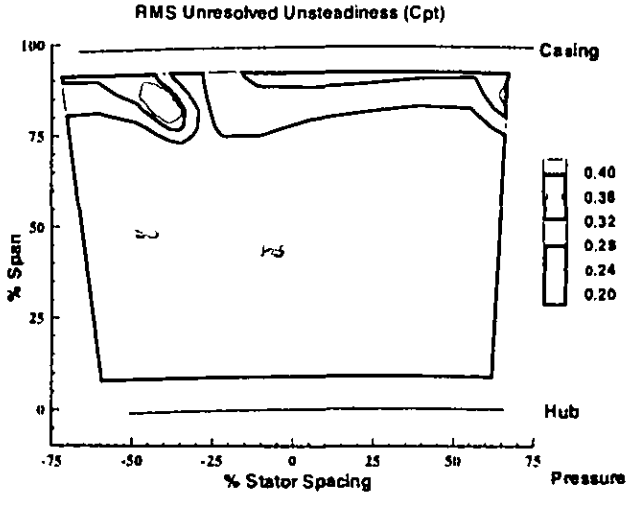

(d) RMS Unresolved Unsteadiness (Cpt)

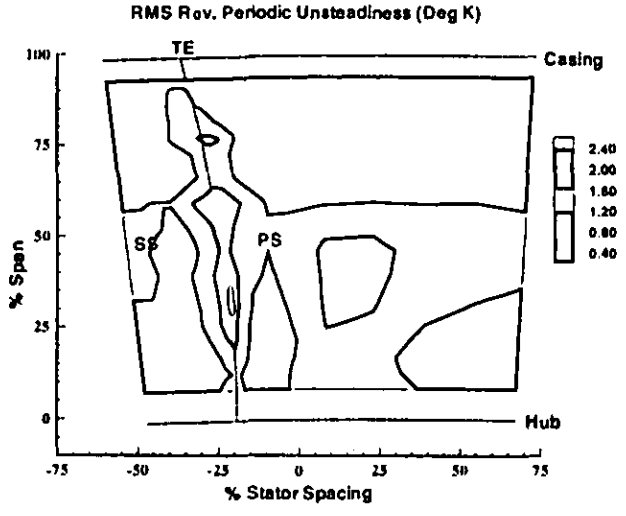

(e) RMS Revolution Periodic Unsteadiness (Deg K)
Total Temperature

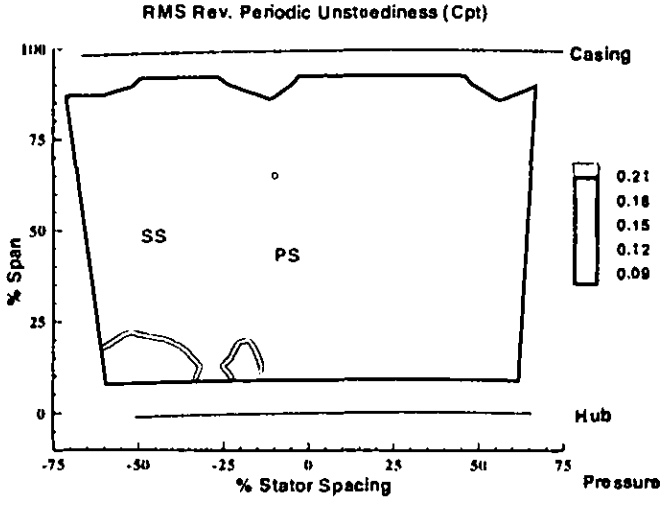

(f) RMS Revolution Periodic Unsteadiness (Cpt)
Total Pressure (Cpt)

Figure 7. Contours of RMS unsteadiness in total temperature compared with total pressure (Cpt).

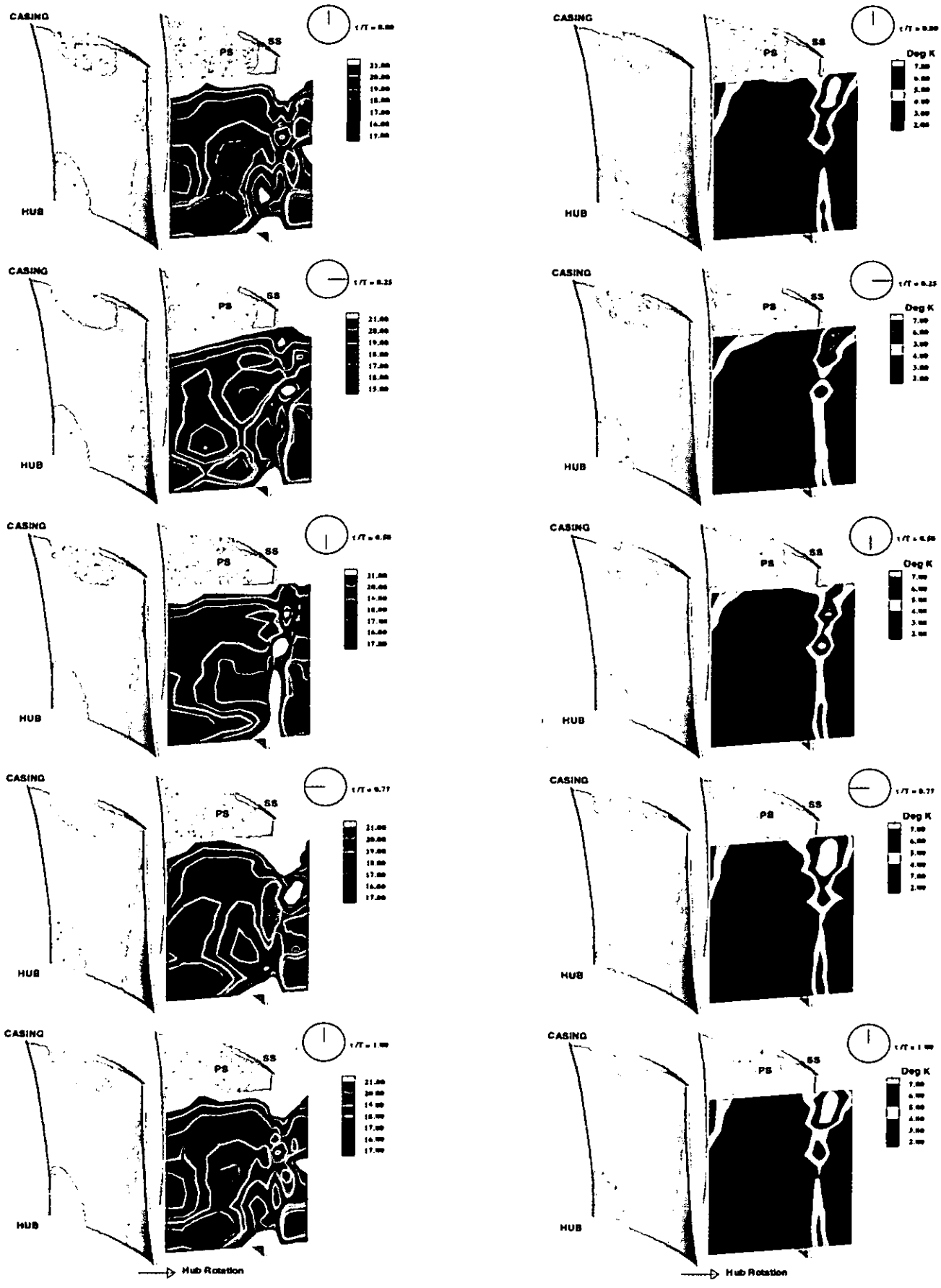

Figure 8. Temporal variation of stator exit flow

at the exit of the stator at the mid-pitch location (32.7% pitch at mid-span) is presented. The ensemble averaged data acquired at the midpitch location of the area traverse is used to explain this flow field. Contour plots of the ensemble averaged total temperature and unresolved unsteadiness in total temperature compared with the ensemble averaged and unresolved unsteadiness in total pressure derived from the high frequency total pressure probe is shown in Figures. 9(a) - (d) respectively. Four blade passages are shown in each plot and the same blade passages are shown in all the plots. For each of these plots, the rotor wake location is identified by the higher total temperature and pressure as well as by the higher unresolved unsteadiness. There seems to be a phase shift between the pressure and temperature wakes. This is possibly due to slight variations in the trigger locations since these measurements were taken a year apart or due to differential probe lengths which will change the local flow around the probes. In any case by shifting the data relative to each other (a constant shift for the entire revolution), the wakes can be made to align. Comparing the ensemble averaged results, it is clear that both total temperature and total pressure wakes are present at this axial location. Since the data is at midpitch, the interaction of the rotor 2 wake with the stator is minimal. Consequently a very clear wake is seen. The flow is also fairly periodic from blade to blade. A complete revolution plot of these data (not shown in this report), showed a typical 2 nodes per revolution pattern consistent with the difference in blade count between rotors 2 and 1. The wakes are much thicker in the casing endwall region than in the hub region. Also the temperature wakes and pressure wakes have different thickness across the span. This could be due to differential decay rates for the temperature and pressure respectively. An another interesting phenomena is that the rotor wake in the casing endwall region has decayed substantially as indicated in both the temperature and pressure distribution. The rotor wake is lowest in the tip, increasing to very high values near the hub. The rotor wake is distorted as it passes through the stator passage due to differing convection velocity. The wakes are the thickest (as evidenced by the ensemble averaged data) near the hub possibly due to radial inward transport of the rotor wake by the stator flow field due to imbalance between the centrifugal forces and the pressure gradient. The core flow is more clearly seen in the temperature distribution than in the pressure signature for the ensemble average and in the pressure than in the temperature signature for the unresolved unsteadiness. In the unresolved unsteadiness distribution, a much larger total pressure core is seen as opposed to the total temperature distribution. Higher levels of unresolved unsteadiness in the casing endwall region is probably a manifestation of the clearance flow.

Isentropic Efficiency Distribution. Isentropic efficiency has been calculated using equation 14 for the ensemble averaged pressure and temperature distribution (one rotor revolution each) at the midpitch location. This is the location away from the endwalls downstream of the stator which has the least influence on the rotor flow. Instantaneous efficiency cannot be calculated since the pressure and temperature measurements have been made at different times. It has to be remembered here that the efficiency calculated in this section is for two stages and is not calculated on a streamline. As a result, the efficiency numbers could be higher than 100%. The overall efficiency calculated using the mass averaged total temperature and pressure downstream of stator 2 referenced to the compressor inlet conditions is 89.5% compared with the overall isentropic efficiency of 89.3%. The uncertainty in the computed efficiency is about $\pm 0.25\%$. An algebraic averaged (across the passage) efficiency (at each radial location) was calculated for each blade passage in the revolution and Fig. 10(a) shows the radial variation of this average efficiency for each blade passage. This picture depicts the bandwidth of efficiency variation across the rotor revolution. There is significant variation in the efficiency of each of the rotor blades. The average bandwidth is about 5% with the maximum variation being around 10%. The possible reasons for the change in efficiency across the rotor revolution are: different incidences, loading changes, influence of the aperiodicity brought about by the differing blade count (seen in the complete rotor revolution contours) etc. Low efficiency numbers are present in the hub and casing endwall regions. The presence of rotor tip clearance flow and stator hub clearance flow and their mixing is probably the main cause of drop in efficiency in these regions. From the designer's viewpoint, it would be desirable to have all the blades perform with the same efficiency. By radially averaging the efficiency for each blade passage, it is possible to look at the best, worst and average blade. For this compressor, if all the blades in rotor 2 behaved as the "best" blade there would be an improvement in efficiency by about 1.3%. It should also be mentioned that the best blade was about 2.5% more efficient than the worst blade. The radial variation of efficiency for the best, worst and average blade is shown in Fig. 10(b). The efficiency of the best blade is better than the average blade at almost all radial locations except close to the endwalls where the efficiencies are almost the same.

Blade to blade distributions of ensemble averaged and blade periodic isentropic efficiency calculated from the temperature and pressure distributions at the midpitch circumferential location is shown in Fig. 10(c) and (d) respectively. For both the distributions, 3 radial locations are shown and at each location 4 blade passages are shown for the ensemble average and 1 blade passage for the blade periodic efficiency, respectively. The locations of the rotor wake can be easily identified as those that have low efficiency. The efficiency distributions are fairly periodic from blade to blade but they do change substantially in the radial direction. The efficiency is very low near the casing. This is partly due to the use of a mass averaged total pressure and total temperature at the inlet and partly due to the large flow mixing that is occurring in the casing endwall region due to the rotor clearance flow.

Composite Flow Field. An attempt was made to determine the composite picture of the rotor exit flow field downstream of stator 2 at the mid-span, mid-pitch location by correlating the unsteadiness in total temperature distribution with the unsteady total pressure data acquired using the kulite probe and the unsteady velocity distributions acquired using the slanted hot-film probe

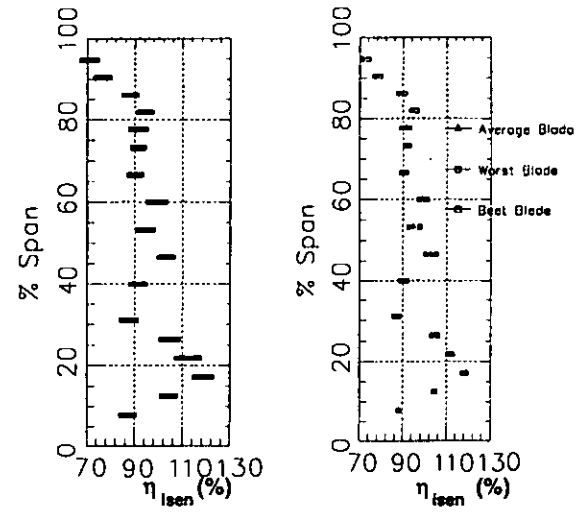

(a) Bandwidth of Efficiency

(b) Best, Worst and Average Blade

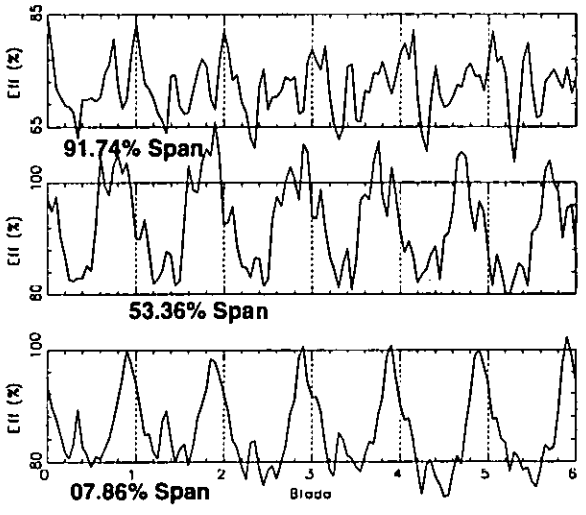

(c) Ensemble Average

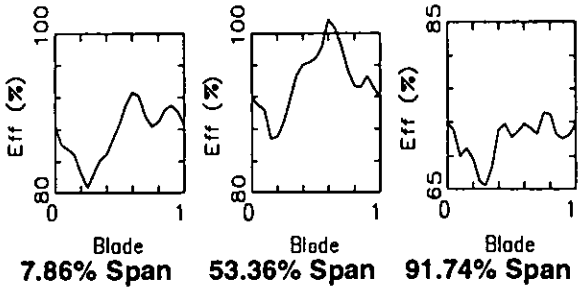

(d) Blade Periodic

Figure 10. Isentropic efficiency distribution at midpitch

with four rotations. Details of the hot-film measurement are given in Prato (1996). Blade-to-blade distributions of ensemble averaged, blade periodic properties and RMS unresolved unsteadiness in total pressure and temperature are shown in Fig. 11. Six blade passages of an ensemble averaged revolution are shown for the ensemble average and unresolved unsteadiness and one blade passage for the blade periodic distribution. For the rotor exit flow in the absolute frame of reference, the wake is defined as the region which has lower axial velocity, higher absolute tangential velocity and higher radial velocity. Depending on the velocity triangles, the total pressure could be higher or lower in the wake. At the location shown, the velocity triangles indicate that the total pressure and total temperature are higher in the wake as the absolute tangential velocity is higher in the wake. In each of these figures, the location of the wake for each of the blade passages is also shown. Since the data is acquired with respect to the trigger on the compressor shaft, it is expected that the ensemble average does indeed show the same wake location. There seem to be small discrepancies in the location of the wake (within 5% of the blade passage) between the velocity, pressure and temperature data. This seems acceptable considering the data has been acquired at different times and the pitchwise resolution of each of these probes is different (hot-film has the best resolution whereas the kulite has the worst). From these figures it is clear that the rotor wake is visible in all the data sets. The axial location of measurement is 130% chord downstream of the rotor. Hence, it is reasonable to expect that the rotor wake has decayed and widened considerably. Larger inter-passage oscillations are found in the total pressure data than in the either the velocity or temperature data sets. This is possibly due to a much higher frequency response of the kulite probe compared with the aspirating and hot-film probes and differing measuring techniques. The wake widths from each of the measurements are approximately the same (approximately. 60% of the passage). This is surprising considering the pitchwise resolution of these instrumentation are different. The pressure and suction surfaces of the wake are marked on the temperature data. In all the data sets a sharper wake is seen on the pressure side and a broader wake on the suction side. This is one more piece of evidence regarding the ability of the aspirating probe to measure total temperature fluctuations and wake widths very accurately.

CONCLUDING REMARKS

Some remarks based on the area traverse of an aspirating probe downstream of second stator are:

1. Higher total temperatures and higher levels of deterministic unsteadiness on the pressure side of the stator confirms the transport of rotor exit flow to the pressure side of the downstream stator.

2. The suction surface casing endwall corner region has high levels of unresolved unsteadiness and is also a region of low efficiency which is probably due to corner stall, inlet skew and casing corner flow as well as intense mixing of the rotor leakage flow, rotor wake and stator endwall flow.

3. The unresolved unsteadiness levels are much higher than the deterministic unsteadiness in the endwall regions and only

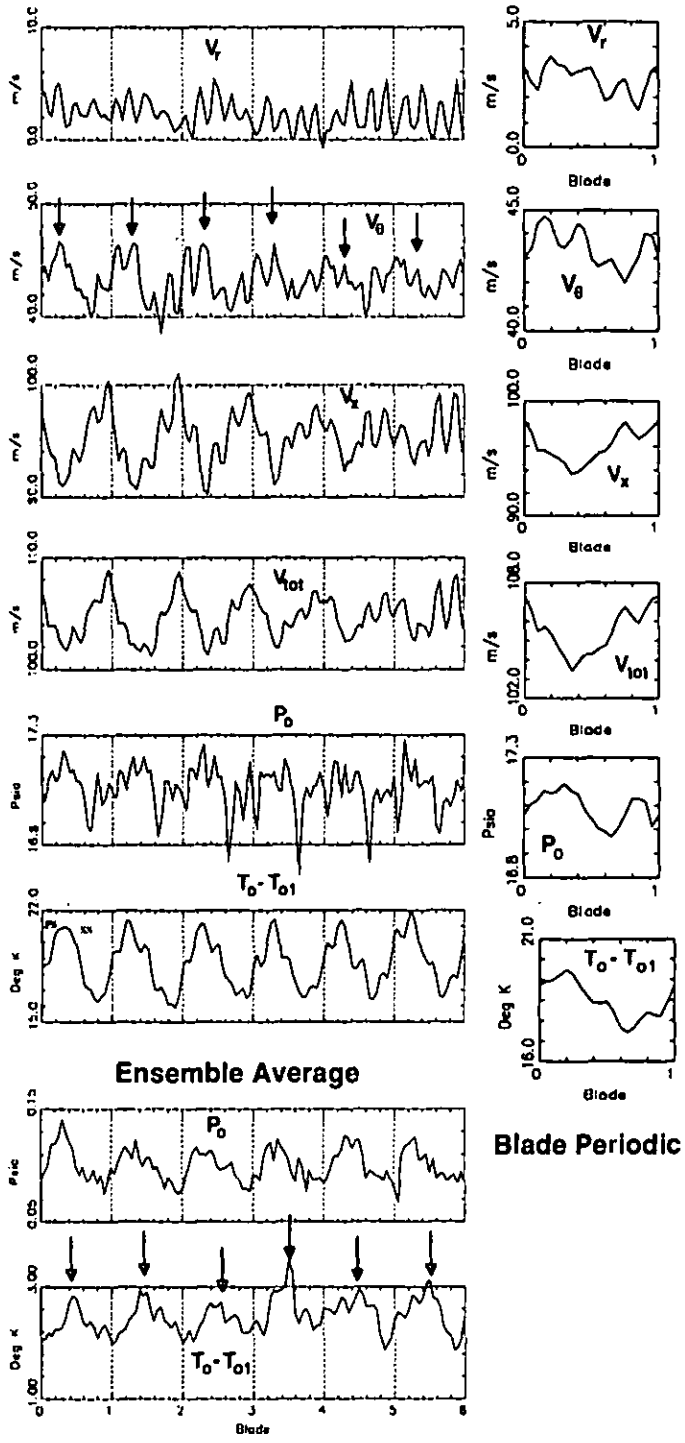

Figure 11. Composite flow field at the midspan, mid-pitch location: Blade-to-blade distribution

marginally higher than the deterministic unsteadiness at mid-span.

4. Regions of high levels of total unsteadiness (stator wakes and casing endwall regions) are also regions of very low efficiency. Thin stator wakes and elimination of casing end-wall corner flow regions is one of the keys to increasing the efficiency of the compressor.

5. Thickening of the rotor wakes near the hub was possibly due to radial inward transport of the rotor wake by the stator flow field due to imbalance between the centrifugal forces and the pressure gradient.

6. At the midpitch location of measurement downstream of the stator, if all the rotor blades were behaving as a "best" blade, the improvement in isentropic efficiency of the compressor would be about 1.3%.

7. As the rotor passes across the stator passage, there are dramatic changes in the flow behavior. They are summarized below:

   - The presence of thick stator wakes and the largest extant of the casing endwall corner region is an indication of the maximum interaction time.
   - As the rotor passes the stator leading edge, the stator wakes start increasing in size and the corner region starts reducing in size. The hub leakage flow region starts contracting in the circumferential direction and starts moving radially. Some of the stator hub wall flow is then transported across the stator passage and deposited on the pressure surface of the stator.

From this study it is clear that significant levels of unsteadiness exist downstream of an embedded stage and that majority of this is due to interaction of rotor 2 wakes with the stator flow field. The interaction of rotor wakes which have both deterministic and unresolved unsteadiness with the stator exit flow which is mainly unresolved in nature (shedding of vorticity from the stator trailing edge due to a time varying circulation on the stator caused by the passage of the rotor wake flow over the stator surfaces) tends to overshadow the interaction between the rotor 2 wake flow and the rotor 3 potential field as evidenced by the low values of the revolution aperiodic unsteadiness (a measure of the rotor/rotor interaction). Development of computational tools which solve the combined stator rotor flow fields are what is needed for the design of future compressors.

ACKNOWLEDGEMENTS

This project was supported by a grant from NASA Lewis Research Center (NAG3-1222 with Dr. A. J. Strazisar as technical monitor), Rolls Royce plc (Mr. M. A. Howard), Rolls Royce Inc. (Mr. R. Moritz) and the Allison engine company (Dr. J. R. Fagan). Helpful suggestions and discussions by these personnel is acknowledged. The authors wish to acknowledge Dr. Wing Ng of VPISU for having provided the design of the aspirating probe and for the helpful suggestions and discussions, Mr. Dale Van Zante of Iowa State for providing useful suggestions and the

methodology of measurement and Mr. H. Houtz of Penn State for having fabricated the aspirating probe. The authors also wish to acknowledge United Technologies Research Center (UTRC) / Pratt & Whitney Aircraft Division of United Technologies Corporation for donating the multistage compressor facility to Penn State.

REFERENCES

Adamczyk, J. J., 1985, "Model Equation for Simulating Flows in Multistage Turbomachinery," ASME Paper No. 85-GT-226.

Alday, J., et al., 1993, "Flow Randomness and Tip Losses in Transonic Rotors," ASME Paper No. 93-GT-189.

Cherrett, M. A., et al., 1994, "Unsteady 3D Flow in a Single-Stage Transonic Fan. Part II: Unsteady Stator Exit Flow Field," ASME Paper No. 94-GT-224.

Howard, M. A., et al., 1993, "Endwall Effects at Two Tip Clearances in a Multi-stage Axial Flow Compressor with Control Diffusion Blading," ASME Paper No. 93-GT-299.

Kerrebrock, J. L., and Mikolajczak, A. A., 1970, "Intra-Stator Transport of Rotor Wakes and Its Effect on Compressor Performance," *ASME Journal of Engineering for Power*, pp. 359–368.

Kotidis, P. A., and Epstein, A. H., 1991, "Unsteady Radial Transport in a Transonic Compressor Stage," *ASME Journal of Turbomachinery*, Vol. 113, pp. 207–218.

Lakshminarayana, B., et al., 1994, "Experimental Investigation of Flow Field in a Multistage Axial Flow Compressor," ASME Paper No. 94-GT-455.

Ng, W. F., 1990, Private Communication.

Ng, W. F., and Epstein, A. H., 1983, "High Frequency Temperature and Pressure Probe for Unsteady Compressible Flows," *Review of Scientific Instruments*, Vol. 54, No.12, pp. 113–124.

Prato, J. P., 1996, *Steady and Unsteady Flow in an Embedded Stator Stage of a Multistage Axial Flow Compressor*. PhD thesis, The Pennsylvania State University.

Prato, J. P., et al., 1995, "Experimental Investigation of the Mean Flow Field at the Exit of an Embedded Stator in a Multistage Axial Flow Compressor," Presented at the ISABE Conference in Melbourne, Australia.

Suder, K. L., et al., 1987, "Measurements of the Unsteady Flow Fields Within the Stator Row of a Transonic Axial Flow Fan, Part I: Measurement and Analysis Technique," ASME Paper No. 87-GT-226.

Suryavamshi, N., et al., 1994, "Unsteady Total Pressure Field Downstream of An Embedded Stator in a Multistage Axial Flow Compressor," Presented at the Winter Annual Meeting of the ASME - ASME AD-Vol. 40 Unsteady Flows in Aeropropulsion, pp. 61–76.

Suryavamshi, N., 1996, *Unsteady Flow, Spanwise Mixing and Rotor-Stator Interaction in Multistage Axial Flow Compressors*. PhD thesis, The Pennsylvania State University.

Van Zante, D. E., et al., 1994, "An Improved Aspirating Probe for Total Temperature and Total Pressure Measurements in Compressor Flows," ASME Paper No. 94-GT-222.